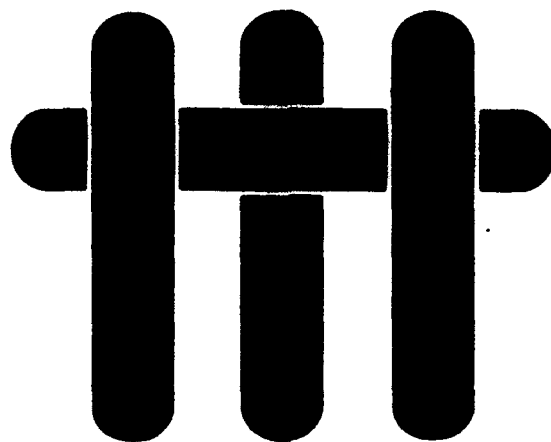


AD-A277 928



2

M A T E R I A L S



DTIC
ELECTE
APR 12 1994
S F D

ON THE MECHANICS OF MICROBALLOON- REINFORCED METAL MATRIX COMPOSITES

This document has been approved
for public release and sale; its
distribution is unlimited.

M.Y. He, B. Wu and F.W. Zok

Materials Department
University of California
Santa Barbara, California 93106

94-10836



4698

N00014-93-1-0224

Submitted to Mechanics of Materials

April, 1994

DTIC QUALITY INSPECTED 3

9 4 4 8 042

ABSTRACT

The elastic/plastic response of ceramic microballoon reinforced metal matrix composites subject to uniaxial loading are examined using finite element analysis. The microballoons are assumed to be spherical and their morphology characterized by the ratio of wall thickness, t , to radius, R . The key parameters investigated are the relative wall thickness, t/R , the modulus ratio (matrix/ceramic) and the yield and hardening characteristics of the matrix. The emphasis of the study is on the overall stress-strain response of the composite, the development of matrix plasticity and the development of stress within the microballoon.

Accession For		1
NTIS	CRA&I	<input checked="" type="checkbox"/>
DTIC	TAB	<input type="checkbox"/>
Unannounced		<input type="checkbox"/>
Justification		
By		
Distribution /		
Availability Codes		
Dist	Avail and/or Special	
A-1		

DEMO QUALITY UNCLASSIFIED 8

1. INTRODUCTION

A novel class of light-weight metal matrix composites (MMCs), utilizing ceramic microballoons as reinforcements, has recently emerged^{1,2}. The microballoons are essentially thin-walled spherical shells, ranging in size from $\sim 20 \mu\text{m}$ to several mm. Typically, the volume fraction of microballoons is in the range of 50-60%. A micrograph of one such composite is shown in Fig. 1. The composites are being targeted for marine applications requiring high specific strength and stiffness and high damping capacity. The potential advantages of these systems over continuous fiber reinforced materials include superior mechanical isotropy, lower production costs and greater flexibility in component fabrication. Their main advantage over conventional particulate-reinforced MMCs is their reduced density, a result of the void space within the reinforcements.

The present paper examines the elastic/plastic response of microballoon reinforced MMCs subject to uniaxial loading (compressive or tensile). The majority of the results are based on a finite element analysis of axisymmetric unit cells. The key parameters investigated are: (i) the ratio of the matrix modulus, E_m to that of the ceramic, E_c ; (ii) the microballoon morphology, characterized by the ratio of wall thickness, t , to microballoon radius, R ; and (iii) the work hardening characteristics of the matrix. The focus of the work is on the overall stress-strain response of the composite, the development of matrix plasticity and the development of stresses within the microballoons.

2. NUMERICAL MODEL

Finite element calculations were conducted on cylindrical unit cells containing a microballoon at the cell center. The height of the cylinder was taken to be equal to the diameter. The ratio of the microballoon wall thickness, t , to the microballoon radius, R ,

was varied from 0 to 1. In all cases, the total volume fraction of microballoons was 50%. A typical finite element mesh for $t/R = 0.2$ is shown in Fig. 2.

The boundary conditions were prescribed to model a state of uniform tension or compression, applied parallel to the axis of the cylinder. The top face of the cylinder was required to remain planar, with an average normal traction, σ , and zero shear traction. The lateral face was also required to remain planar but with zero average normal and shear tractions acting on it. The model was implemented using the finite element program ABAQUS, with 8-noded 2-dimensional axisymmetric biquadrilateral elements. A typical mesh contained 480 elements and 1565 nodes. The overall strain was increased by increments of $\Delta\epsilon/\epsilon_0 = 0.1$ for $\epsilon/\epsilon_0 < 5$, $\Delta\epsilon/\epsilon_0 = 0.2$ for $5 < \epsilon/\epsilon_0 < 10$, and $\Delta\epsilon/\epsilon_0 = 0.5$ for $\epsilon/\epsilon_0 > 10$. The effective (deviatoric) strain in the matrix as also evaluated, allowing the evolution of matrix plasticity with remote strain to be monitored. In addition, the stresses within the microballoon were evaluated.

In most cases, the matrix material was taken to be elastic-perfectly plastic, with a yield stress σ_0 . In others, the matrix was assumed to follow power-law hardening, in accordance with the Ramberg-Osgood flow law. For uniaxial loading, this law can be expressed as

$$\frac{\epsilon}{\epsilon_0} = \frac{\sigma}{\sigma_0} + \alpha \left(\frac{\sigma}{\sigma_0} \right)^n \quad (1)$$

where ϵ_0 is the yield strain (σ_0/E_m); σ and ϵ are the axial stress and strain, respectively; α is a numerical coefficient, taken to be 3/7; and n is the work hardening exponent. The effects of matrix hardening were studied by varying n between 0 and 0.2. The solid portion of the microballoon was assumed to be elastic, with a Young's modulus, E_c . The Poisson's ratios ν of both the matrix and the microballoon material were taken to be 0.3.

The onset of particle cracking was assumed to occur when the maximum tensile stress within the microballoon reached a critical value, σ_c .

3. ELASTIC PROPERTIES

3.1 Numerical Results

Figures 3(a) and (b) show the effects of the modulus ratio, E_c/E_m , and the microballoon morphology, characterized by the ratio t/R , on the composite modulus. In (a), the results are normalized by the matrix modulus, E_m , and, in (b), by the limiting composite modulus, E_s , corresponding to $t/R = 1$. The limiting modulus E_0 at $t/R = 0$ is $0.330 E_m$. The latter limit corresponds to a porous material (with no reinforcement) and is thus independent of E_c/E_m . At the other limit, wherein $t/R = 1$, the modulus E_s increases monotonically with the modulus ratio, E_c/E_m . In the regime $0.5 \leq t/R \leq 1$, the modulus is insensitive to t/R , indicating that the elastic response of the microballoons is similar to that of fully dense particulates. When t/R drops below ~ 0.5 , the modulus begins to decrease more rapidly with decreasing t/R . For modulus ratios in the range $2 \leq E_c/E_m \leq 10$, the relative reduction in modulus is essentially independent of the elastic mismatch, E_c/E_m , as shown in Fig. 3(b). For higher values of E_c/E_m , the reduction is less sensitive to t/R .

At the simplest level, the trends in modulus with wall thickness can be rationalized on the basis of the porosity within the microballoon. By interpolating linearly between the two limiting cases (corresponding to $t/R = 0$ and 1), the modulus can be approximated by

$$E/E_m = p E_0/E_m + (1-p) E_s/E_m \quad (2)$$

where p is the volume fraction of porosity within the microballoon and is related to the wall thickness through

$$p = (1-t/R)^3. \quad (3)$$

The predictions of Eqns. (2) and (3) are shown by the dashed lines in Fig. 3(a). For modulus ratios in the range $2 < E_c/E_m < 10$, this approach appears to be consistent with the FEM results. For higher modulus ratios, the two differ substantially over the entire range of t/R , with the FEM calculations yielding higher values of E .

The finite element calculations have also been used to evaluate the Poisson's ratio of the composites, and the results combined with the Young's moduli to evaluate the bulk modulus, k . The trends in k with t/R and E_c/E_m are shown in Fig. 4. Also shown are the results of an analytical solution, described below.

3.2 Analytical Solution

An analytical solution for the bulk modulus of the microballoon composites has been obtained by considering the elastic response of a *spherical* unit cell, subject to hydrostatic loading. The cell consists of a spherical microballoon and a concentric spherical shell of matrix material. The dimensions of the microballoon and the matrix are selected to give a microballoon volume fraction of 50%. The solution is obtained by invoking the usual continuity and equilibrium conditions^{3,4}. The results of this analysis can be expressed as

$$\frac{k}{k_m} = 2(1-2\nu)/\left(5 - 7\nu - 9(1-\nu)^2 \gamma\right) \quad (4)$$

where

$$\gamma = \left\{ 2 - \nu(1 + E_m / E_c) + (E_m / E_c) \left[\frac{(1 - \nu)(2 + (1 - t/R)^3)}{2(1 - (1 - t/R)^3)} \right] \right\}^{-1}$$

Comparisons between the analytical and FEM results are presented in Fig. 4. The two approaches yield similar results, though the analytical results slightly overestimate those from the FEM for $t/R \geq 0.2$. This discrepancy is attributable to the different unit cell shapes (cylinder vs. sphere) used in the two sets of calculations.

3.3 Performance Indices

The design of structural components requires consideration of three factors: (i) the properties of the material, (ii) the component geometry, and (iii) the functional requirements of the component. In many instances, the material is selected on the basis of certain *performance indices*, each characterizing the performance of the material in a certain class of component geometry and functional requirement. For stiffness-critical design, three such indices have been identified⁵. The first is the ratio E/ρ , where ρ is the density of the material. A material with the highest value of this index produces the stiffest rod, subject to axial loading, for a given mass of material. The second is the ratio $E^{1/2}/\rho$. This performance index is used for the optimal design of a beam in bending or a column subject to elastic buckling. The third index, $E^{1/3}/\rho$, is used for the design of plates, loaded in bending, either externally or by self-weight.

These performance indices have been used to assess the stiffness characteristics of microballoon composites relative to those of the matrix material alone. For this purpose, three *normalized* performance indices are introduced: $E \rho_m / E_m \rho$, $E^{1/2} \rho_m / E_m^{1/2} \rho$ and $E^{1/3} \rho_m / E_m^{1/3} \rho$, with ρ being the composite density. Alternatively, the normalized indices can be written in the form $(E/E_m)^{1/\alpha} (\rho_m/\rho)$ where α is a

numerical coefficient that can take on values of 1, 2 or 3, depending on the loading configuration. The trends in these indices with the wall thickness, t/R , and the density ratio ρ_c/ρ_m (with ρ_c being the density of the ceramic) for a modulus ratio $E_c/E_m = 5$ are presented in Fig. 5. For low values of ρ_c/ρ_m (< 1), all performance indices are maximized when the reinforcements are fully dense ($t/R = 1$). The indices initially decrease slowly with decreasing t/R . At small values of t/R , the indices decrease more rapidly, with the rate of decrease increasing with the coefficient α , i.e. $E \rho_m/E_m \rho$ decreases more rapidly than $E^{1/2} \rho_m/E_m^{1/2} \rho$. For $\rho_c/\rho_m = 1$, the optimal wall thickness depends on the performance index of interest. Specifically, for $\alpha = 1$, the performance index is maximized at $t/R = 1$; for $\alpha = 2$, it remains essentially constant over the entire range of t/R ; and for $\alpha = 3$, it is maximized at $t/R \approx 0.05$. For yet higher values of ρ_c/ρ_m , the performance index for $\alpha = 1$ becomes more insensitive to t/R , though it is still maximized at $t/R = 1$. The other two indices are at a maximum at $t/R = 0$ and at a minimum at $t/R = 1$.

The results demonstrate that the selection of the ceramic/metal combination and the relative wall thickness for optimal stiffness characteristics depends sensitively on the intrinsic physical and mechanical characteristics of the constituents as well as the application under consideration. Moreover, assessment of the performance of the composites relative to that of the matrix material alone can be readily made through the use of appropriate *normalized* performance indices.

4. PLASTIC FLOW AND FRACTURE

4.1 Elastic/Plastic Response

The stress-strain curves of composites in the elastic-plastic regime for $t/R = 0.5$ and 0.05 are shown in Figs. 6(a) and (b). Also shown in the figures are the boundaries between the elastic and yielded regions of the matrix at various levels of overall strain.

The stress-strain curves for composites encompassing the entire range of t/R (0 to 1), over a wide range of strains are shown in Fig. 7.

For composites with thick walled microballoons ($t/R = 0.5$), matrix yielding initiates in the polar regions (above and below the microballoon), and spreads laterally with increasing strain (Fig. 6). The onset of yielding occurs at an overall strain which is less than the matrix yield strain ($\epsilon/\epsilon_0 < 1$). The matrix becomes fully yielded at an overall strain, $\epsilon/\epsilon_0 \approx 1.5$, corresponding to a stress, $\sigma/\sigma_0 \approx 1.5$. Nevertheless, the flow stress of the composite continues to increase with strain, reaching a saturation level, $\sigma/\sigma_0 = 1.75$, at a strain, $\epsilon/\epsilon_0 \approx 6$ (Fig. 7). The development of matrix yielding and the asymptotic approach to the saturation flow stress are essentially the same as those previously found for composites reinforced with *fully dense* spherical particulates ($t/R = 1$)⁶.

The behavior of composites containing thinner walled microballoons is substantially different. For $t/R = 0.05$, matrix yielding initiates in regions located $\sim 30^\circ$ away from the equatorial plane of the microballoon (Fig. 6). This occurs at a relatively small strain: $\epsilon/\epsilon_0 \approx 0.6$. Upon further loading, the yielded region quickly spreads toward the equatorial plane and, somewhat less quickly, toward the polar region. The elastic region within the matrix persists up to large overall strains, i.e. $\epsilon/\epsilon_0 \geq 5$. However, at these strains, the composite flow stress remains relatively small: $\sigma/\sigma_0 \sim 1.0$. Upon yet further loading, the flow stress continues to increase slowly with strain. It ultimately reaches the same asymptotic level as with the thick-walled microballoons ($\sigma/\sigma_0 \approx 1.75$), though at a much larger strain ($\epsilon/\epsilon_0 \approx 30$). With the thin-walled microballoons, the strain range over which transient response persists is extremely large, such that the flow stress measured experimentally in these materials is not expected to reach the saturation level.

4.2 Stress Distributions

Finite element calculations have also been performed to evaluate the stress distributions within the microballoons. Illustrative examples showing the effect of wall thickness are shown in Figs. 8 and 9. In these examples, the remote strain is $\varepsilon/\varepsilon_0 = 2$ and the applied stress is tensile. The stresses are expressed in terms of the cylindrical co-ordinate system (r, θ, z) that defines the external boundaries of the composite unit cell. In addition, the minimum and maximum principal stresses are evaluated. The location and magnitude of the maximum principal stress, S_1 , is used to identify the probable location of microballoon fracture and the corresponding applied stress and strain. Similarly, the minimum principal stress S_3 is used to address the problem of microballoon fracture under remote *compressive* loading.

Under tensile loading, the maximum principal stress in the thick walled microballoons ($t/R = 0.5$) occurs at the inside wall of the microballoon, along the equatorial plane (Fig. 8). Comparisons of the S_1 and σ_{zz} contours indicate that the maximum principal stress in this region acts parallel to the loading direction. Consequently, tensile failure of the microballoons is expected to occur by the formation of cracks along the equatorial plane, perpendicular to the applied stress. For thin-walled microballoons ($t/R \leq 0.2$), the location and direction of the maximum principal stresses are the same (Fig. 9), and consequently the mode of cracking is expected to be similar. Furthermore, the magnitude of the principal stresses in the thin walled microballoons is similar to that in the thick walled microballoons for a prescribed remote strain. As a result, tensile failure is expected to be initiated at a similar strain, though the stresses will differ substantially.

Under compressive loading, the principal stress distribution depends more sensitively on wall thickness. For thick walled microballoons ($t/R = 0.5$), the maximum principal stress (shown as the minimum principal stress for tensile loading) is located

along the inside wall in the polar region of the microballoon (Fig. 8). Comparisons of the S_1 , σ_{zz} , and σ_{rr} contours indicate that these highly stressed regions are essentially in a state of equal biaxial tension, with the stresses acting perpendicular to the loading direction. As a result, cracks are expected to initiate in the polar region and be aligned parallel to the loading direction.

In the thick walled microballoons, the maximum principal stress acting along the outer surface of the microballoon in the equatorial plane is also relatively large. Here, S_1 acts in the hoop direction, with the radial stress σ_{rr} being small and the axial stress σ_{zz} being compressive. Flaws located in these regions could lead to hoop cracks oriented parallel to the loading direction. As the wall-thickness is reduced, the magnitude of the principal stresses in the equatorial regions increase relative to those in the polar region (Fig. 9). Indeed, when t/R drops below ~ 0.2 , the equatorial regions experience the largest principal stress, and are thus expected to be the regions in which cracking is initiated.

The evolution of the maximum principal stress within the microballoon with applied strain for both tensile and compressive loading is summarized in Fig. 7. The results are presented as contours of constant maximum principal stress. As expected, the maximum principal stress develops more rapidly in tension than in compression. Nevertheless, for wall thicknesses in the range, $t/R \leq 0.2$, the maximum principal stress under compressive loading reaches substantial levels ($\geq 5 \sigma_0$) at modest strains ($\sim 5 \epsilon_0$). It is also of interest to note that for compressive loading, the maximum principal stress initially *increases* with increasing t/R at a prescribed overall *strain*, up to $t/R \sim 0.2$. In this regime, the strain required to cause microballoon cracking would decrease with increasing t/R . For $t/R \geq 0.2$, the maximum principal stress decreases with increasing t/R . However, it decreases with increasing t/R at a prescribed remote *stress* for all values of t/R .

At the simplest level, the onset of cracking in the microballoons can be assumed to occur when the maximum principal stress within the microballoon reaches a critical level, σ_* . This criterion can be combined with the computed stress distributions to predict the remote stress for the onset of cracking. Though this stress does not necessarily correspond to composite *fracture*, it does provide a relative measure of performance, incorporating the effects of wall thickness and microballoon strength. The pertinent results from tensile and compressive loadings are summarized in Figs. 10(a) and (b), respectively. Several features concerning flow and fracture are noteworthy. When the microballoons are sufficiently weak ($\sigma_*/\sigma_0 \leq 4$ for tension and $\sigma_*/\sigma_0 \leq 2$ for compression), the microballoons fracture before the limit flow stress is achieved, regardless of wall thickness. In this regime, the composite would be expected to exhibit limited ductility. For stronger microballoons, the limit stress can be achieved prior to the onset of fracture, provided the wall thickness is sufficiently large. In this regime, the material would be expected to exhibit substantially higher ductility, with fracture controlled by an alternate mechanism (e.g. ductile fracture of the metal). The variation in the critical wall thickness with microballoon strength for both tensile and compressive loading is plotted in Fig. 11. The lines in this figure essentially represent transitions in failure mechanisms, from the one dominated by microballoon cracking to the one governed by either ductile rupture of the matrix (for tensile loading) or the attainment of the limit flow stress (for compressive loading).

4.3 Effects of Matrix Hardening

The effects of matrix hardening on the overall stress-strain response of the composite were evaluated by varying the exponent n in the Ramberg Osgood law. Figs. 12(a) and (b) show the flow curves for two values of t/R (0.05 and 0.2) and three values of n (0, 0.1 and 0.2). Fig. 13 shows the same results presented in the normalized form, $\sigma(\epsilon)/\sigma_m(\epsilon)$, where $\sigma(\epsilon)$ is the flow stress of the composite at a strain ϵ and

$\sigma_m(\epsilon)$ is the flow stress of the matrix at the same level of strain. It is apparent that the flow stress of these composites always increases with the hardening exponent, n , as it does in the matrix material alone. However, the flow stress ratio, $\sigma(\epsilon)/\sigma_m(\epsilon)$, exhibits somewhat different behavior. For thick-walled microballoons, $\sigma(\epsilon)/\sigma_m(\epsilon)$ increases with n , as reported previously for particulate reinforced materials⁶. Furthermore, the asymptotic level of this ratio increases with n . In contrast, for the thin-walled microballoons, $\sigma(\epsilon)/\sigma_m(\epsilon)$ decreases with increasing n at small strains ($\epsilon/\epsilon_0 \leq 20$ for $t/R = 0.05$), indicating that the strengthening increment derived from the microballoons (expressed in terms of the average matrix flow stress) is diminished. At larger strains, the trends with n are reversed, and ultimately, the flow stress ratio reaches the same asymptotic level for all values of t/R .

CONCLUDING REMARKS

The elastic/plastic response of microballoon reinforced metal matrix composites has been studied through finite element analysis of a unit cell model. The key parameters governing the response are the normalized wall thickness, t/R , the modulus ratios E_c/E_m and the matrix hardening exponent, n . Moreover, the strength and ductility are governed by the microballoon strength, σ_*/σ_0 .

Clearly, the elastic moduli of materials with $t/R < 1$ are less than those for fully dense particulates ($t/R = 1$), though the former materials have a lower density. In some applications, comparisons of elastic properties on the basis of the normalized performance indices rather than of the modulus itself would be the preferred approach. In this case, the microballoon composites may provide optimal performance, depending on the density ratio, ρ_c/ρ_m , and modulus ratio, E_c/E_m . The plastic response of the microballoon composites exhibits trends similar to those of particulate reinforced

materials, with one important difference: the transient region in the microballoon composites persists to much larger strains, increasing with decreasing t/R .

The attainment of the limit flow stress in the microballoon composites depends on t/R and σ_*/σ_0 , as well as the direction of loading (tension vs. compression). For relatively weak, thin-walled microballoons, fracture of the microballoons is likely to occur at a low level of applied stress and may limit the strength and ductility of the composite. Conversely, for relatively strong, thick-walled microballoons, the limit flow stress may be achieved, though in some instances it may be precluded by other failure mechanisms.

ACKNOWLEDGMENTS

This material is based upon work supported by the Office of Naval Research under Award No. N00014-93-1-0224.

REFERENCES

1. S.P. Rawal and M.S. Misra, "Development of a Ceramic Microballoon Reinforced Metal Matrix Composites," *Proc. 34th Int. SAMPE Symp.*, p. 112, 1989.
2. T.H. Sanders, "Microstructure and Properties of Ceramic Aerosphere Composites," *Proc. Tenth Ann. Mtg. on Discontinuously Reinforced MMC*, Jan. 1988.
3. M. Timoshenko and J.N. Goodier, "Theory of Elasticity," McGraw-Hill Book Company, 1970.
4. G. Bao, to be published, 1994.
5. M.F. Ashby, "Materials Selection in Mechanical Design," Pergamon Press, Oxford, pp. 56-69, 1992.
6. G. Bao, J.W. Hutchinson, R.M. McMeeking, "Particle Reinforcement of Ductile Matrices against Plastic Flow and Creep," *Acta Metall. Mater.*, **39**, pp. 1871-1882, 1991.

FIGURES

- Fig. 1** A scanning electron micrograph of a composite comprised of Al_2O_3 microballoons in an Al alloy matrix.
- Fig. 2** A typical unit cell and finite element mesh ($t/R = 0.2$).
- Fig. 3** Influence of wall thickness and ceramic/matrix modulus ratio on the composite modulus normalized by (a) the matrix modulus, E_m , and (b) the limiting composite modulus, E_* . The dashed lines in (a) are interpolations between the end points, in accordance with Eqn. 2.
- Fig. 4** Comparison of bulk modulus computed from the analytical solutions (solid lines) with those obtained from FEM (dashed lines).
- Fig. 5** Influence of wall thickness on the stiffness performance indices, for density ratios, ρ_c/ρ_m , of (a) 1/3, (b) 1, and (c) 3.
- Fig. 6** The elastic/plastic response and development of matrix yielding for composites with microballoon wall thicknesses, t/R , of 0.5 and 0.05. The regions on the hatched sides of the lines have yielded.
- Fig. 7** Effects of microballoon wall thickness on the axial stress-strain response. The thin lines represent contours of constant maximum principal stress within the microballoon wall: (a) tensile loading, (b) compressive loading. Note that the flow response, indicated by the solid lines, is independent of the mode of loading (tension vs. compression).
- Fig. 8** Stress distribution within microballoon for $t/R = 0.5$. The remote strain is $\epsilon/\epsilon_0 = 2$.
- Fig. 9** Stress distribution in microballoon for $t/R = 0.1$. The remote strain is $\epsilon/\epsilon_0 = 2$.

- Fig. 10 Trends in the stress required for the onset of microballoon cracking with wall thickness, t/R , and normalized microballoon strength, $\bar{\sigma}/\sigma_0$: (a) tension and (b) compression.
- Fig. 11 Variation in the critical wall thickness with microballoon strength for tensile and compressive loading.
- Fig. 12 Effects of matrix hardening on the composite flow response for: (a) $t/R = 0.2$ and (b) $t/R = 0.05$.
- Fig. 13 The normalized flow stress ratio, $\bar{\sigma}(\bar{\epsilon})/\bar{\sigma}_m(\bar{\epsilon})$, for (a) $t/R = 0.2$ and (b) $t/R = 0.05$.



Figure 1

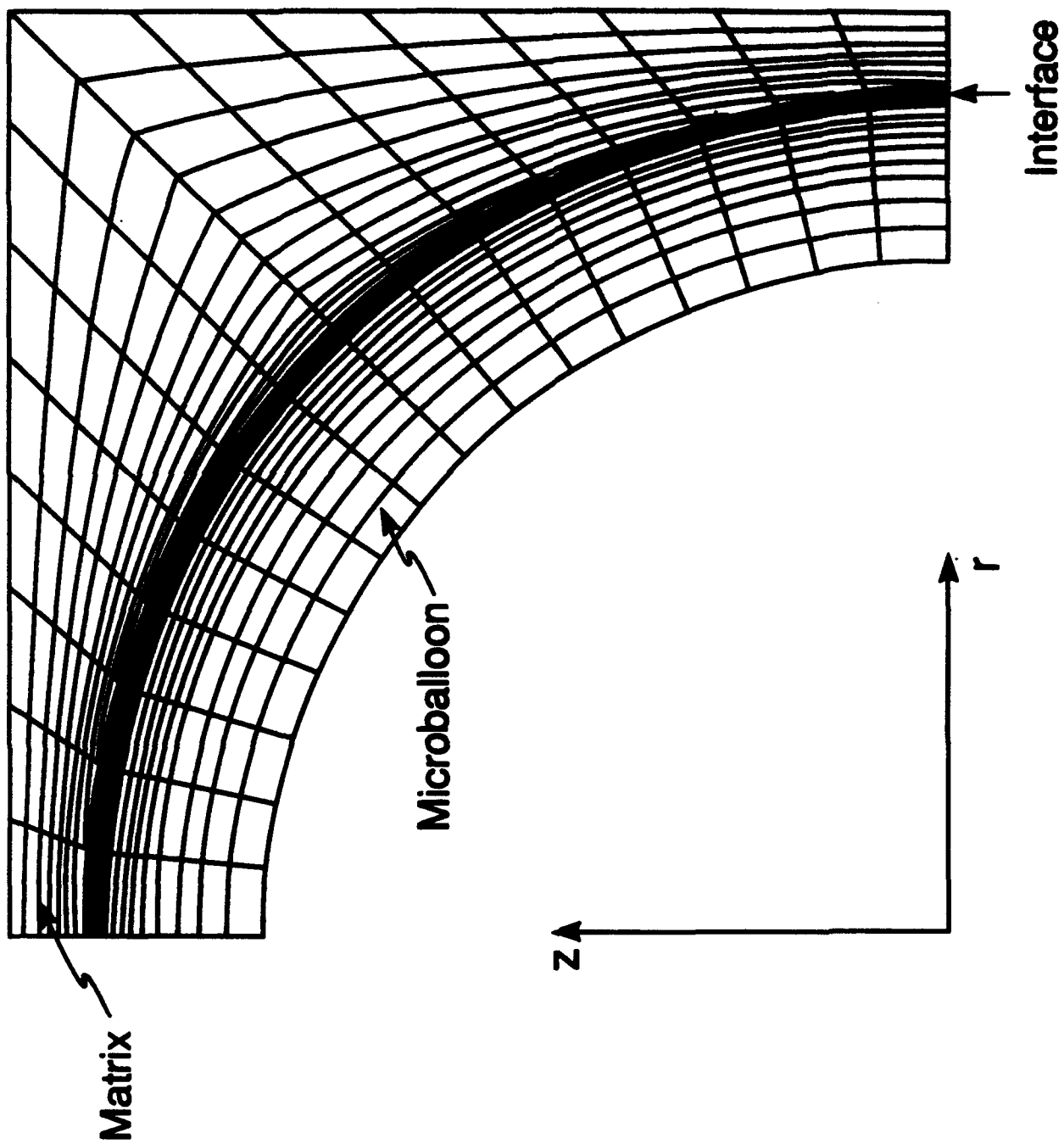


Figure 2

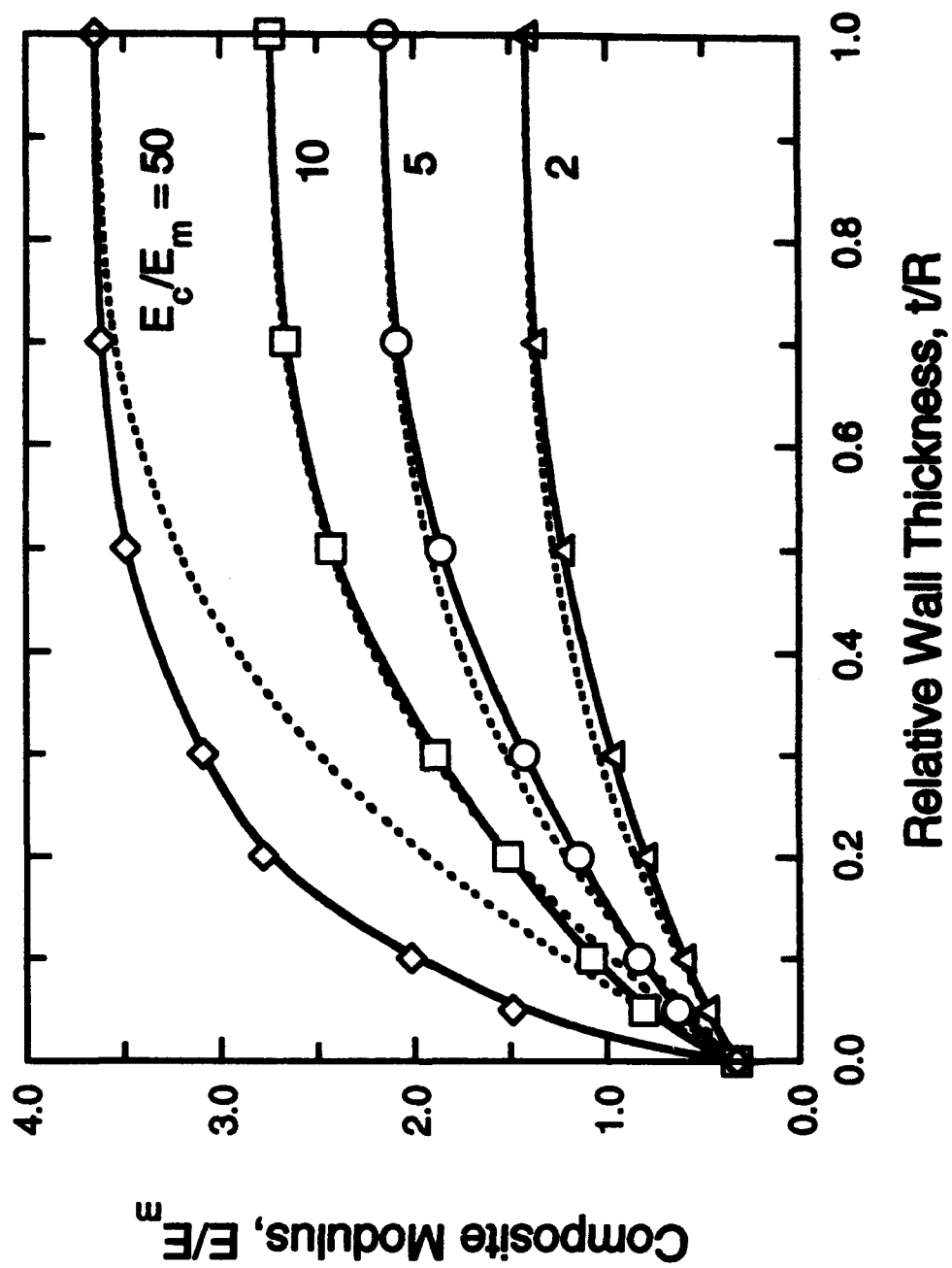


Figure 3(a)

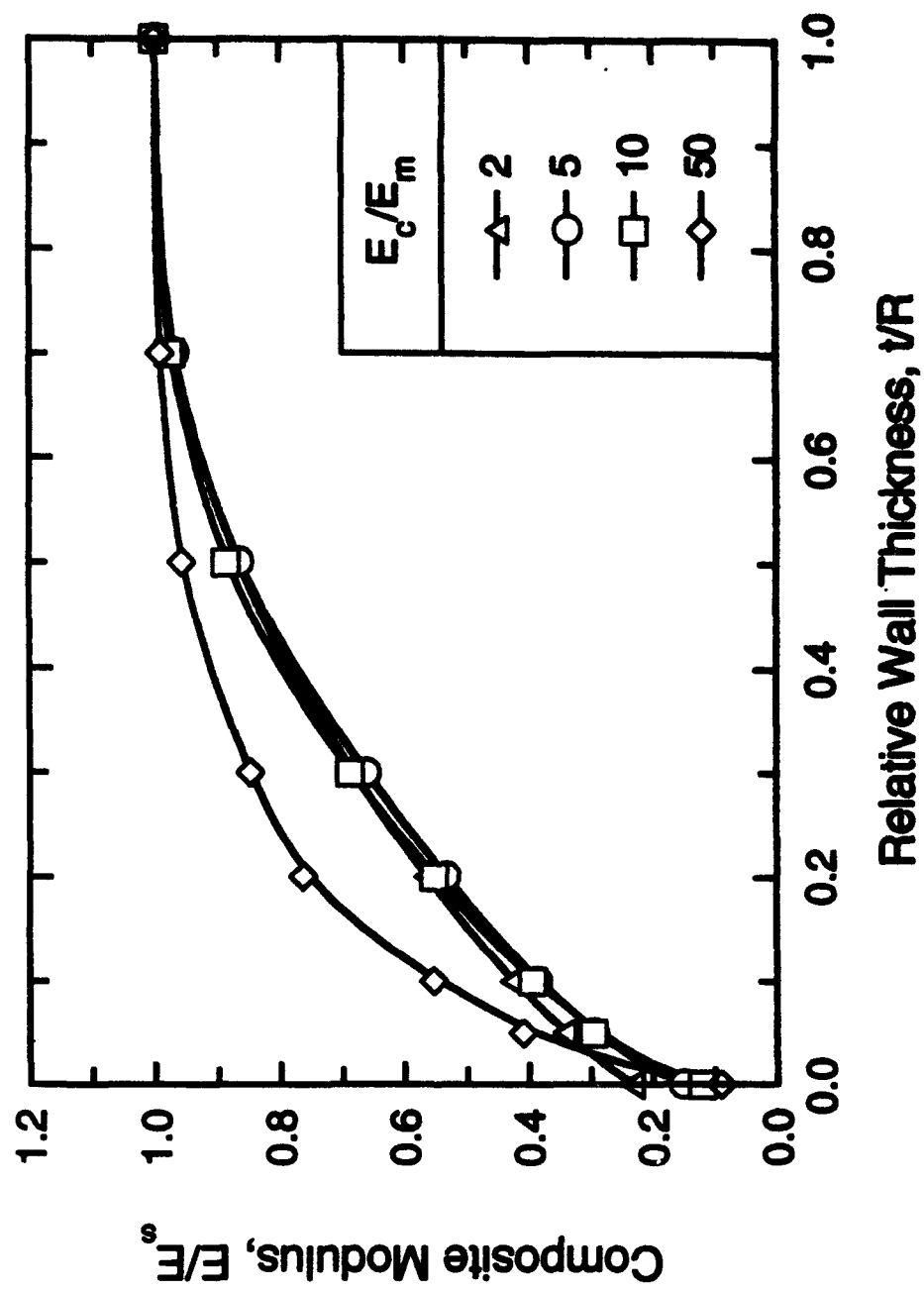


Figure 3(b)

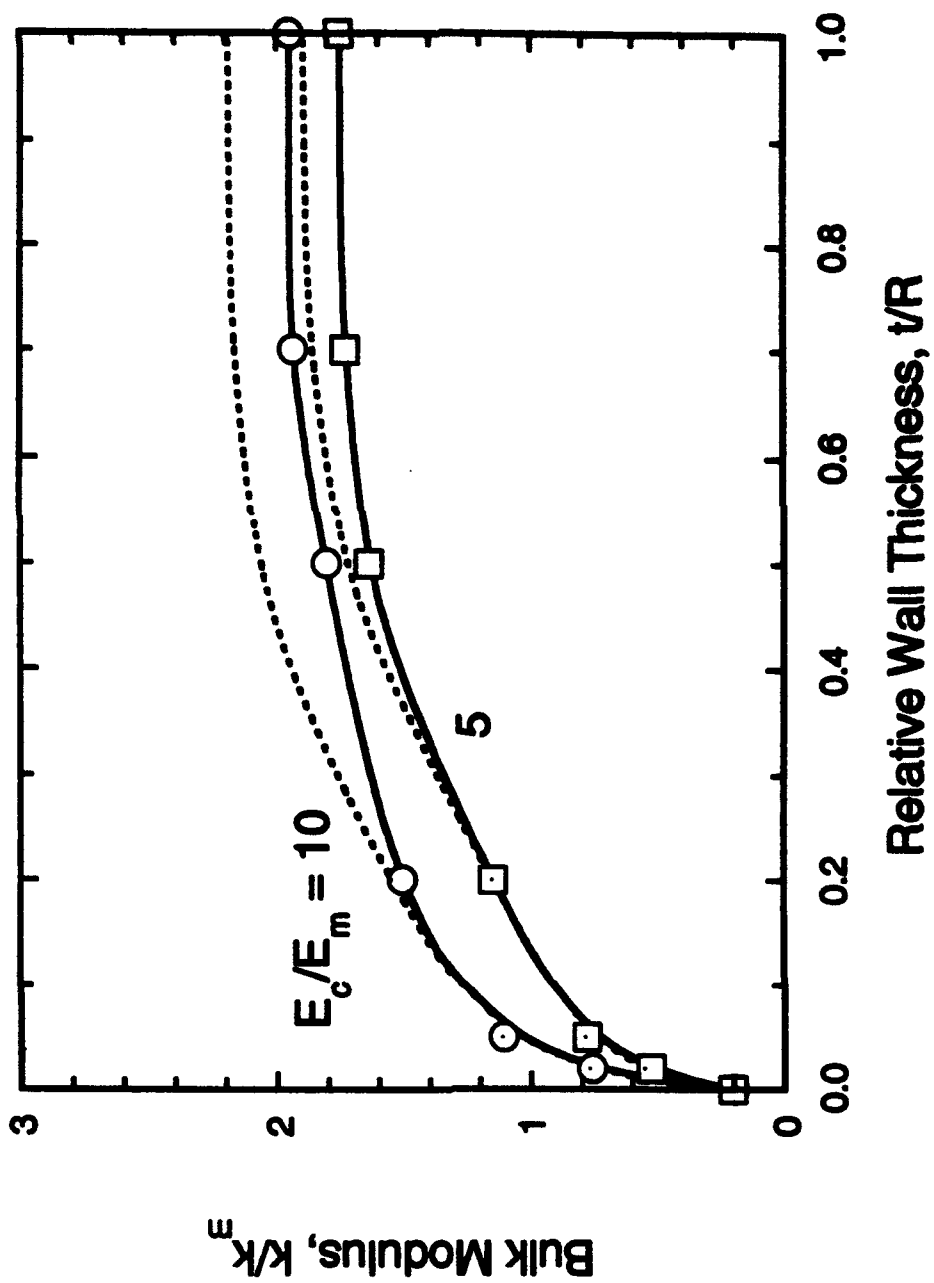


Figure 4

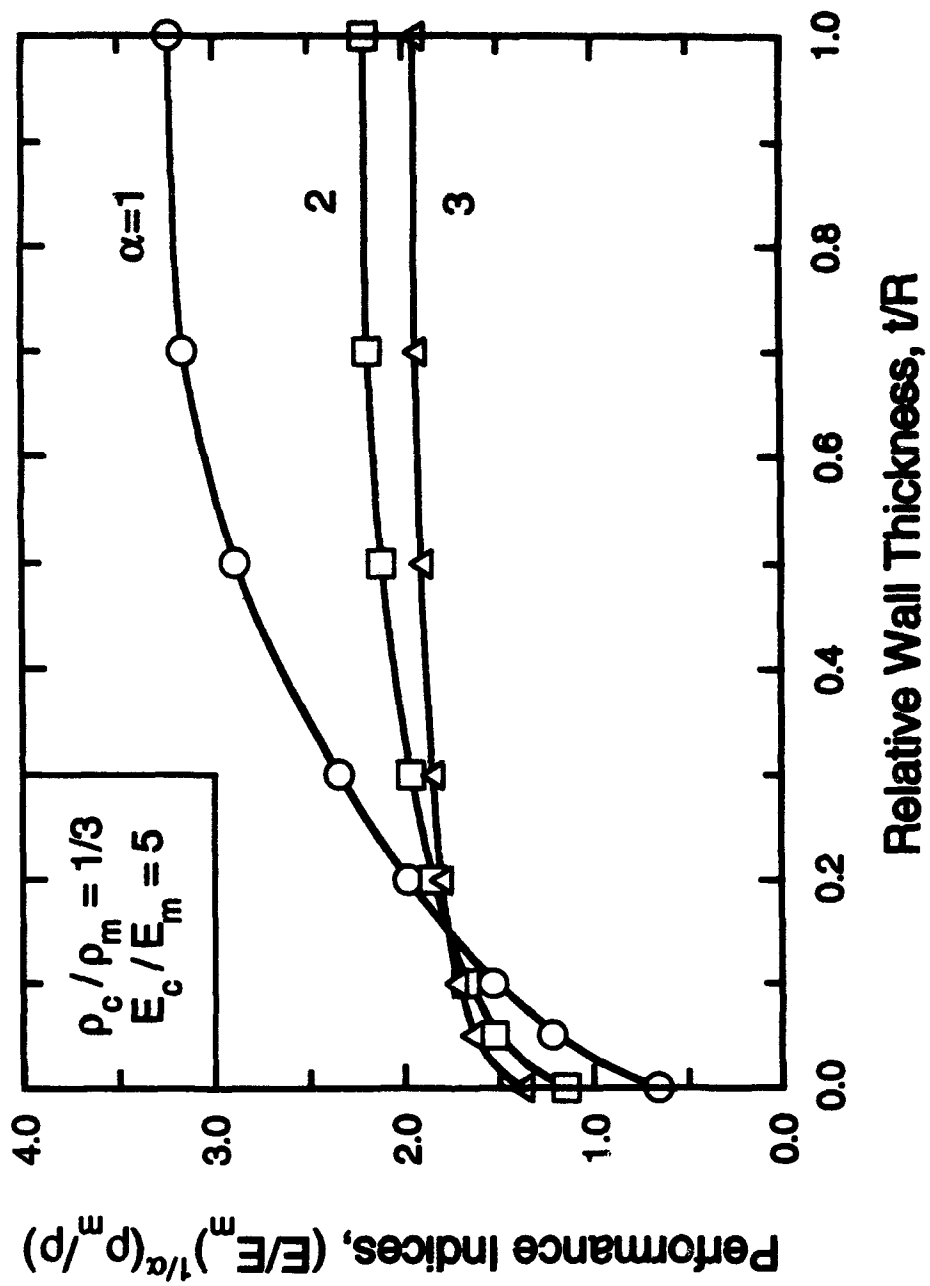


Figure 5(a)

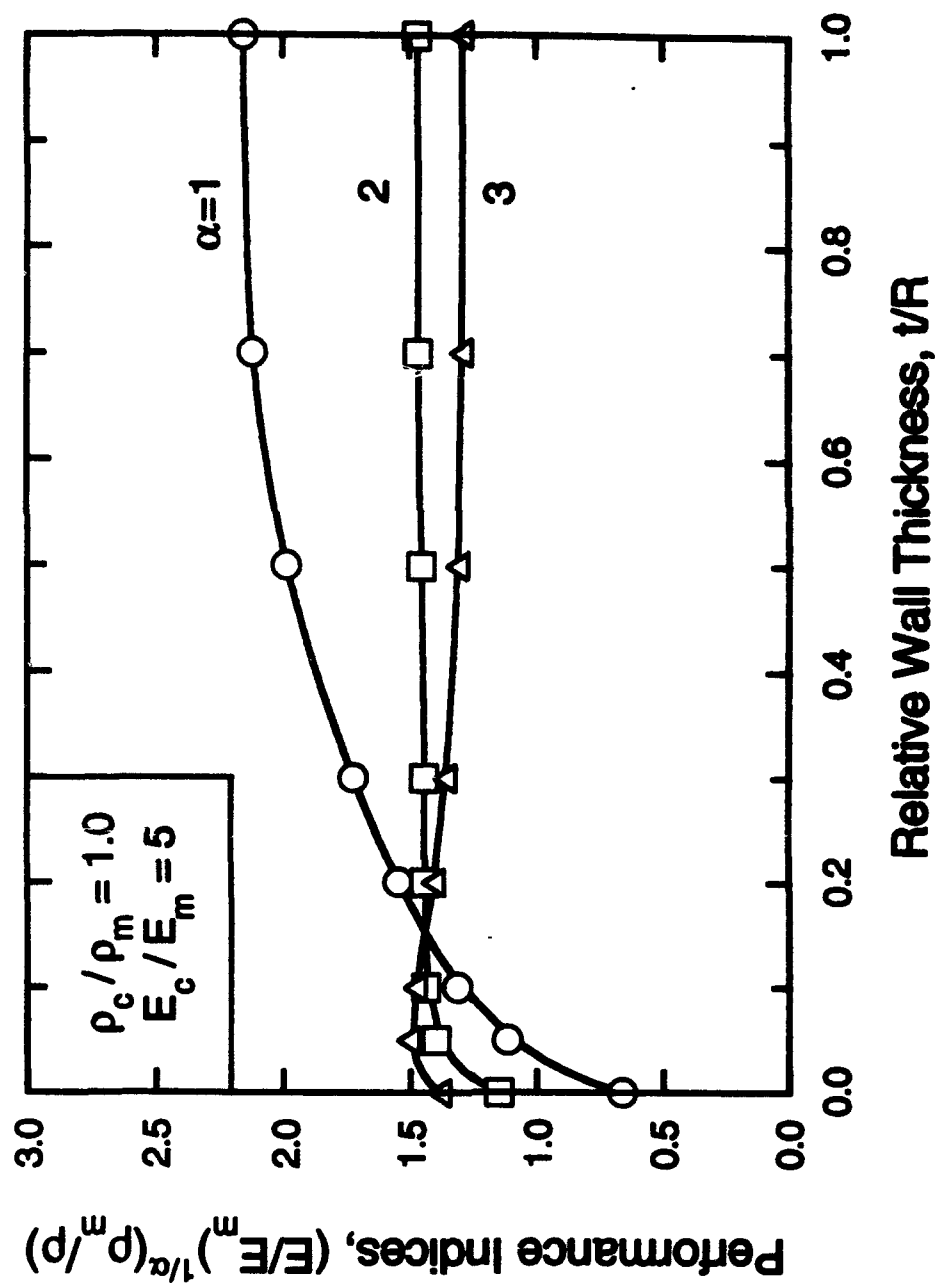


Figure 5(b)

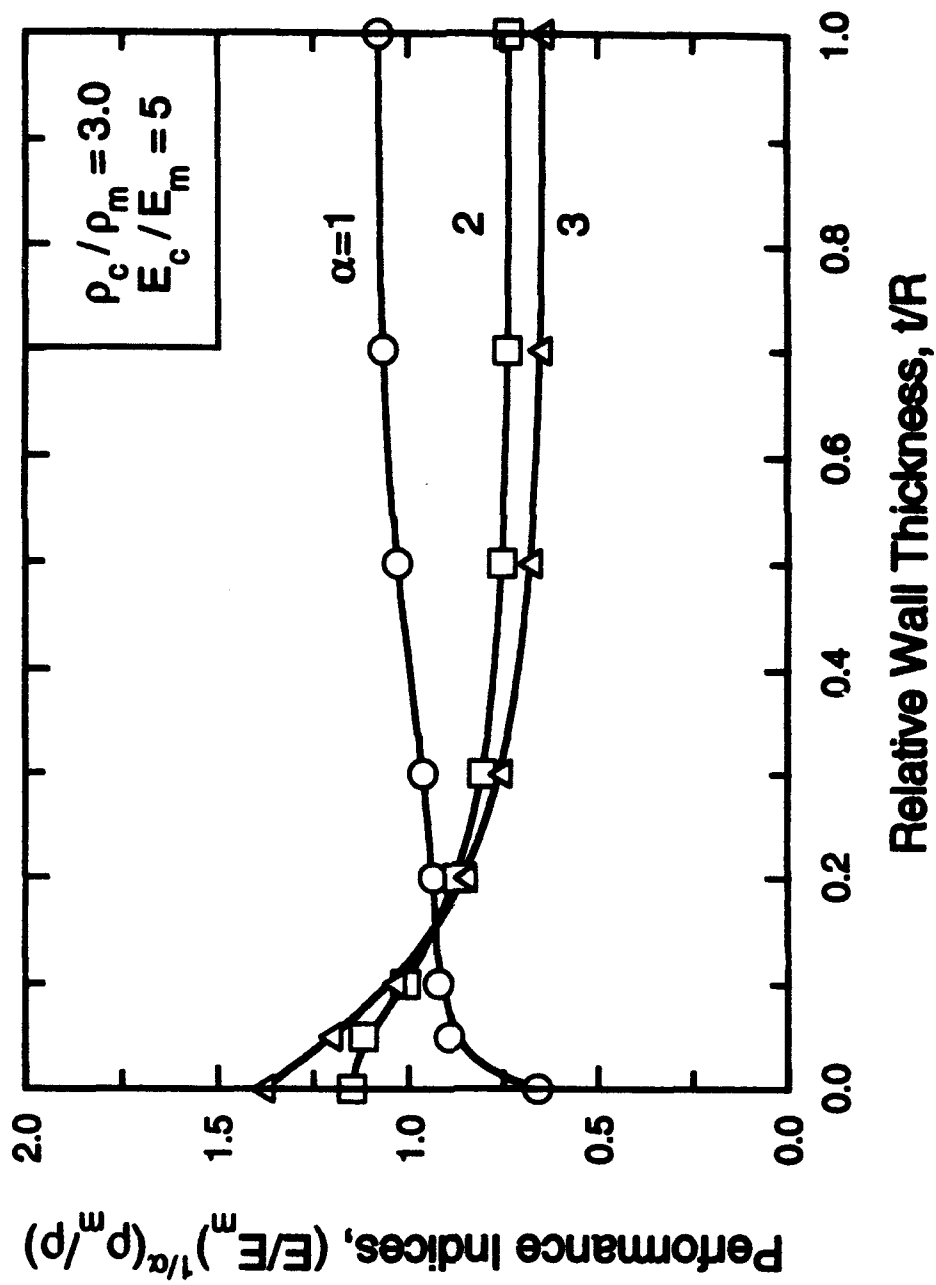


Figure 5(c)

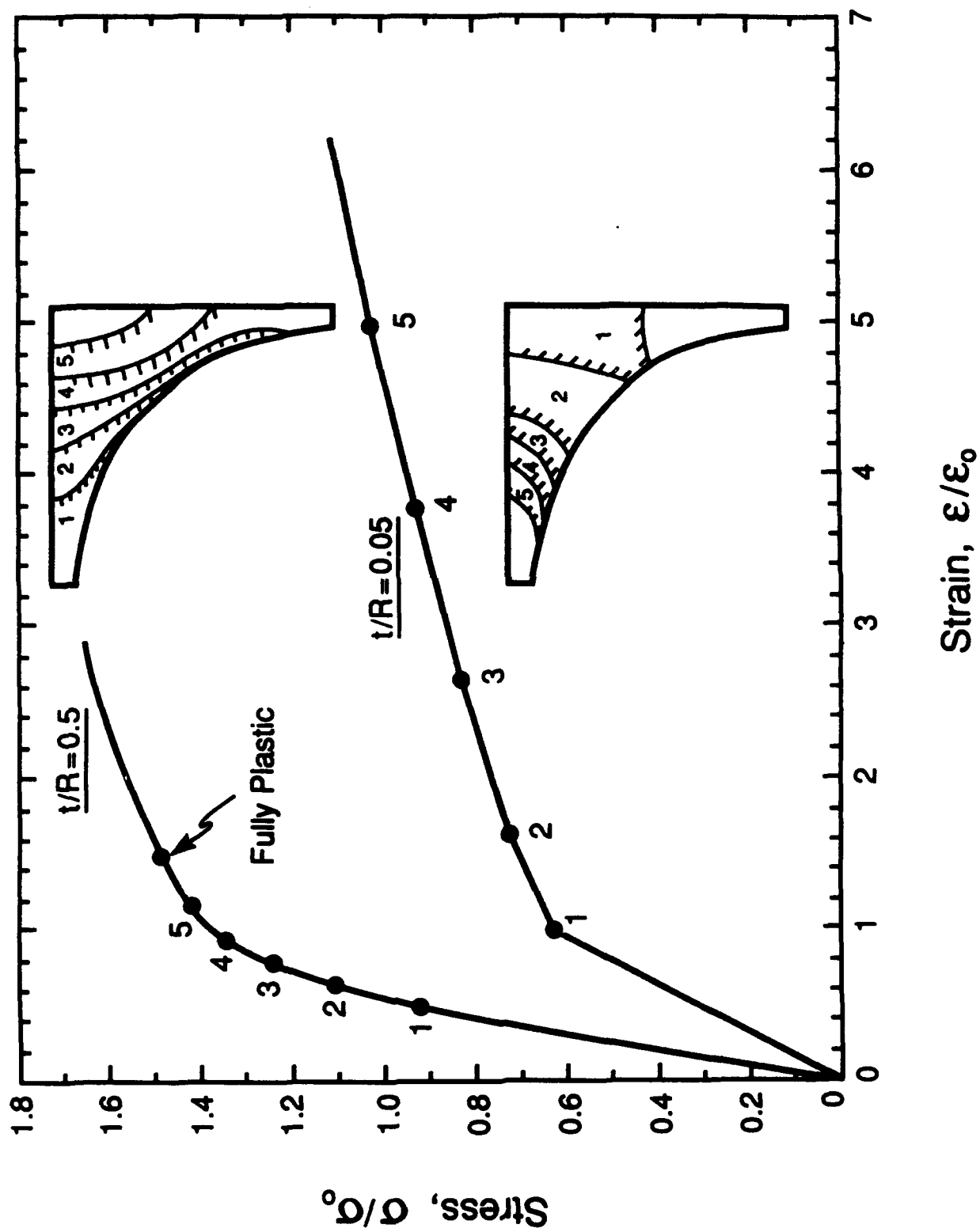


Figure 6

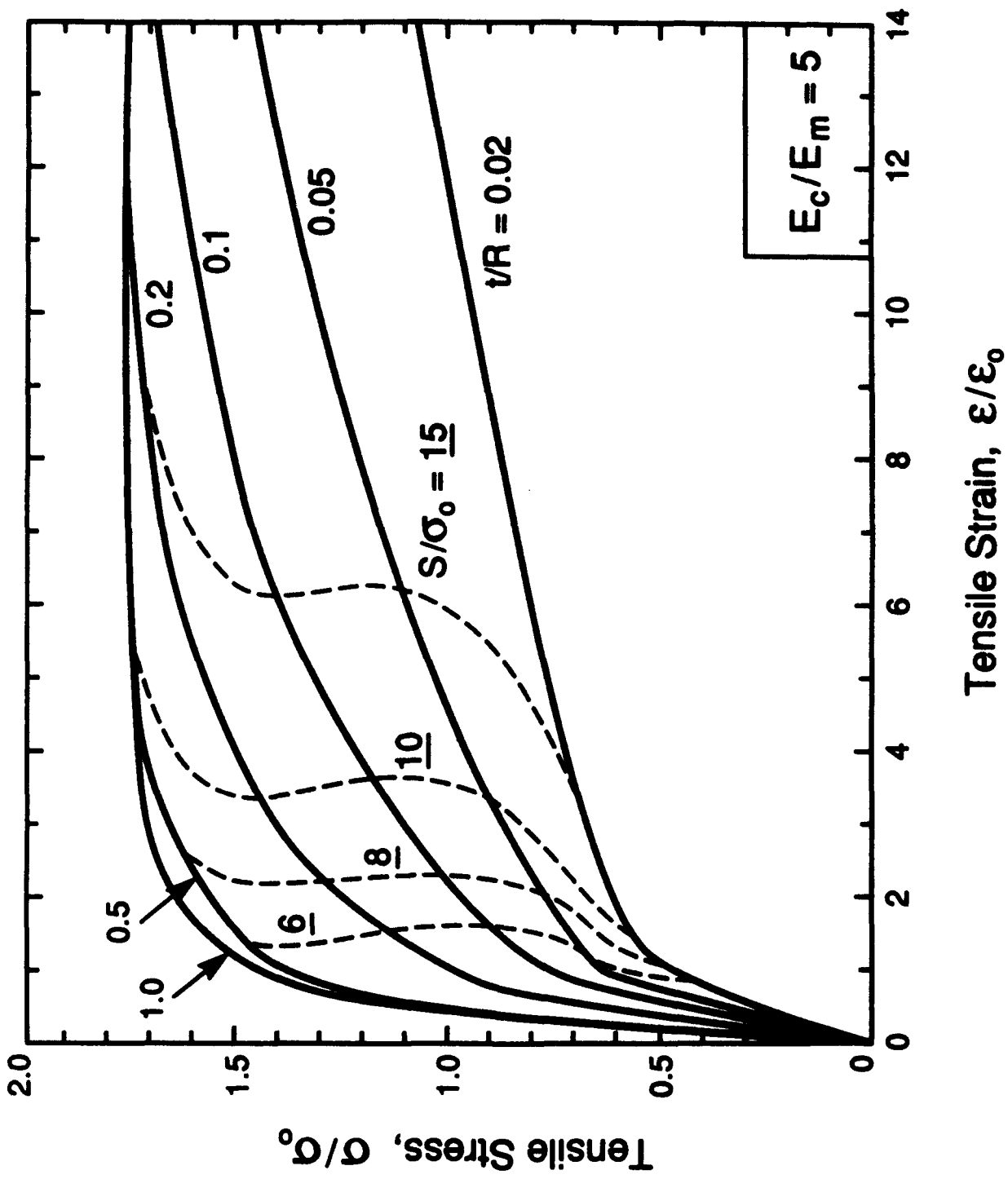


Figure 7(a)

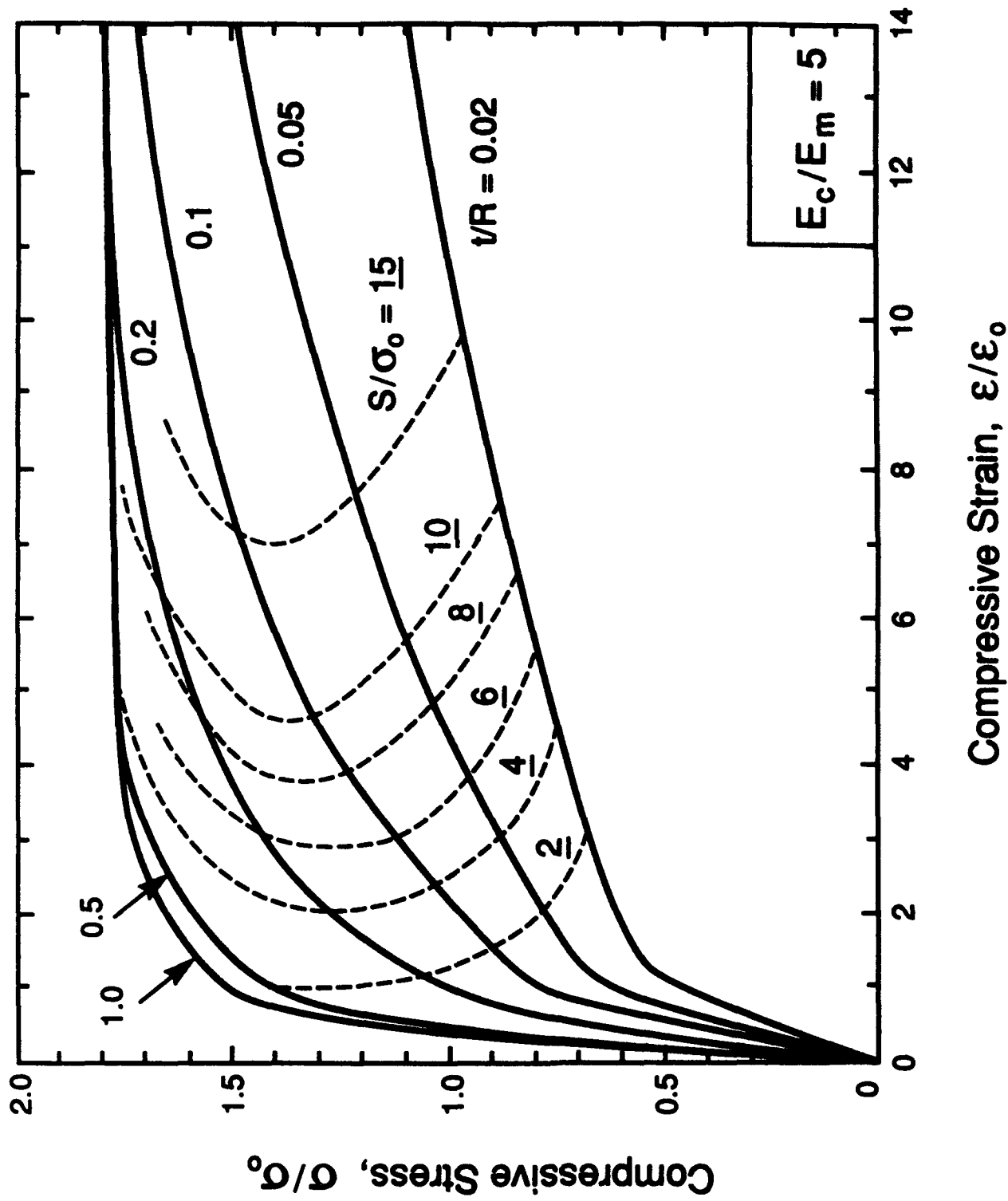


Figure 7b

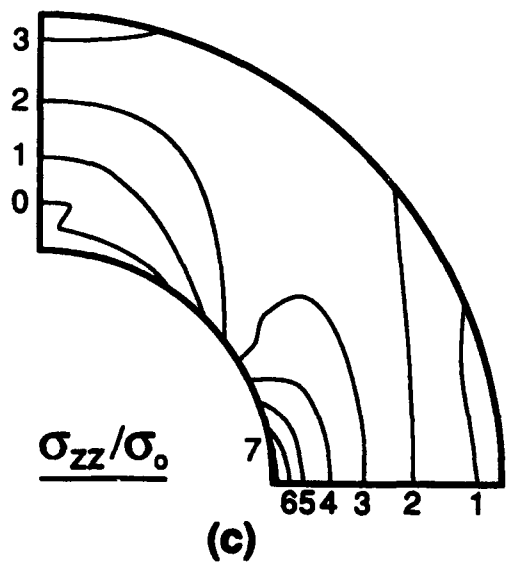
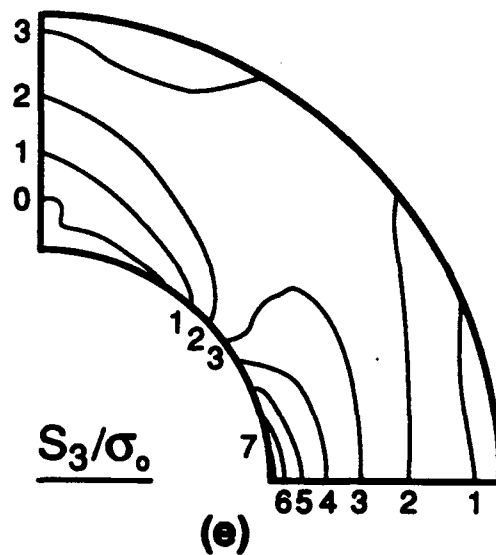
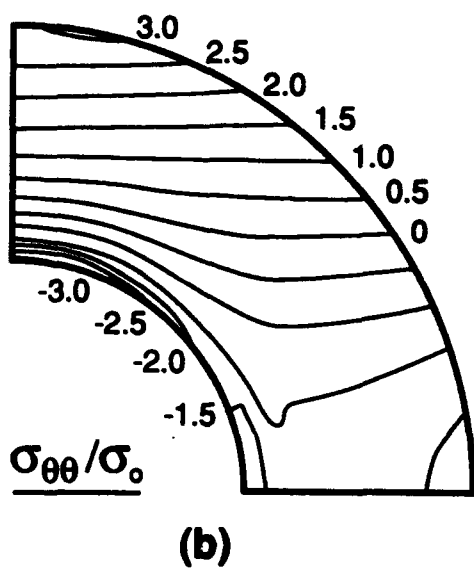
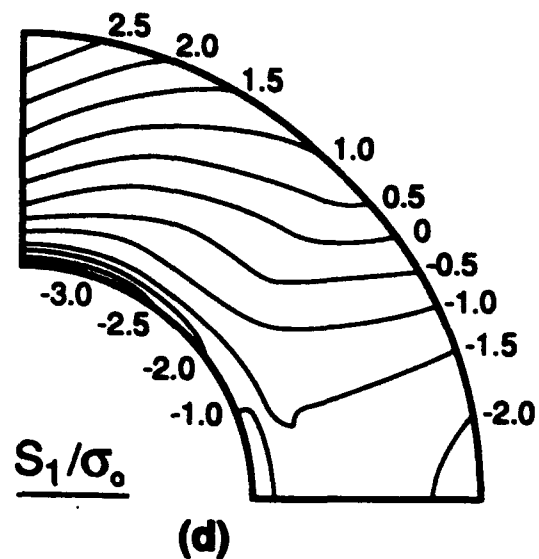
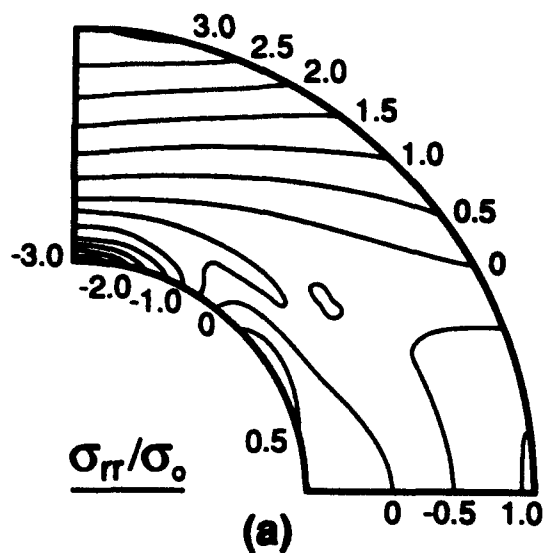


Figure 8

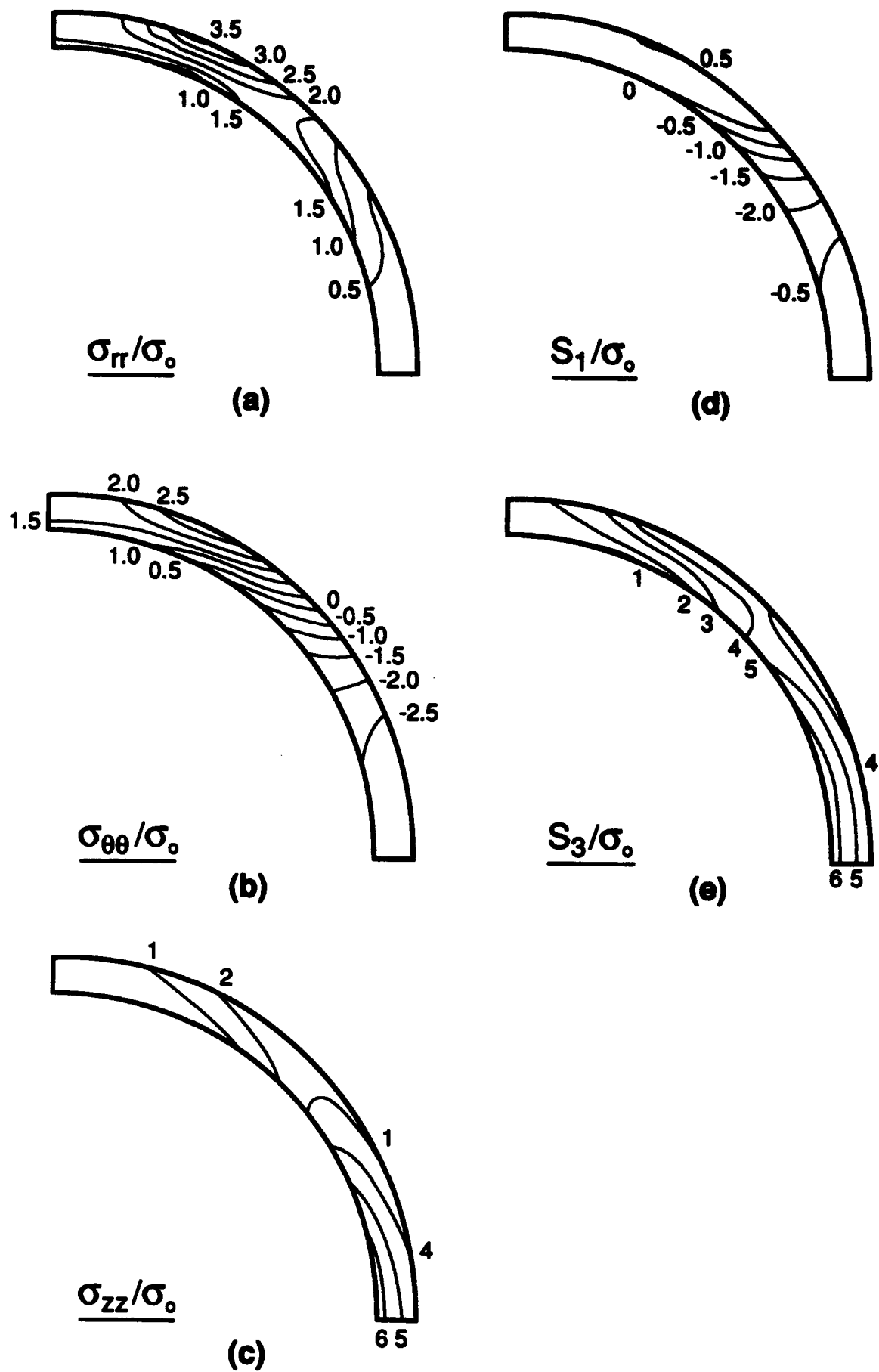


Figure 9

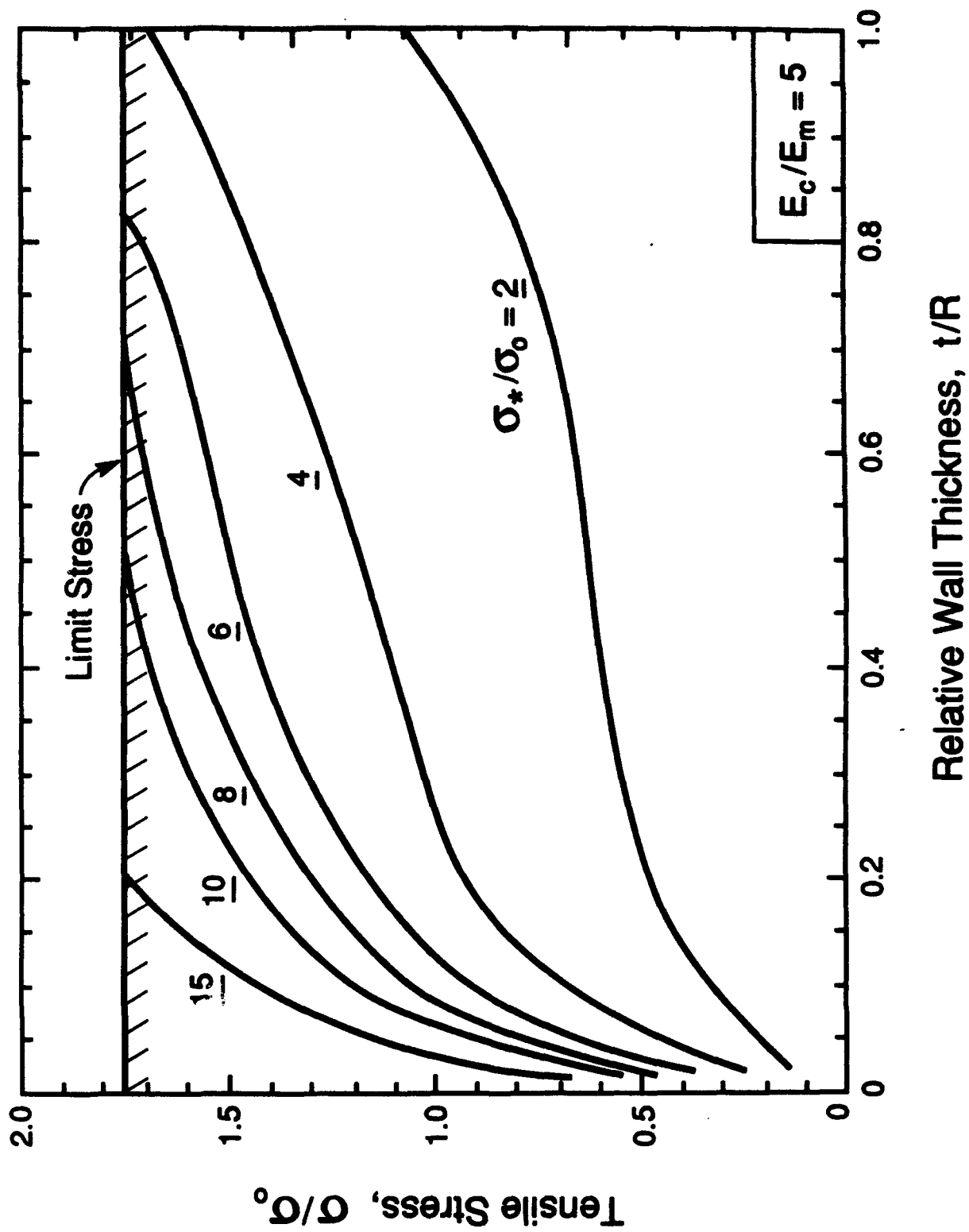
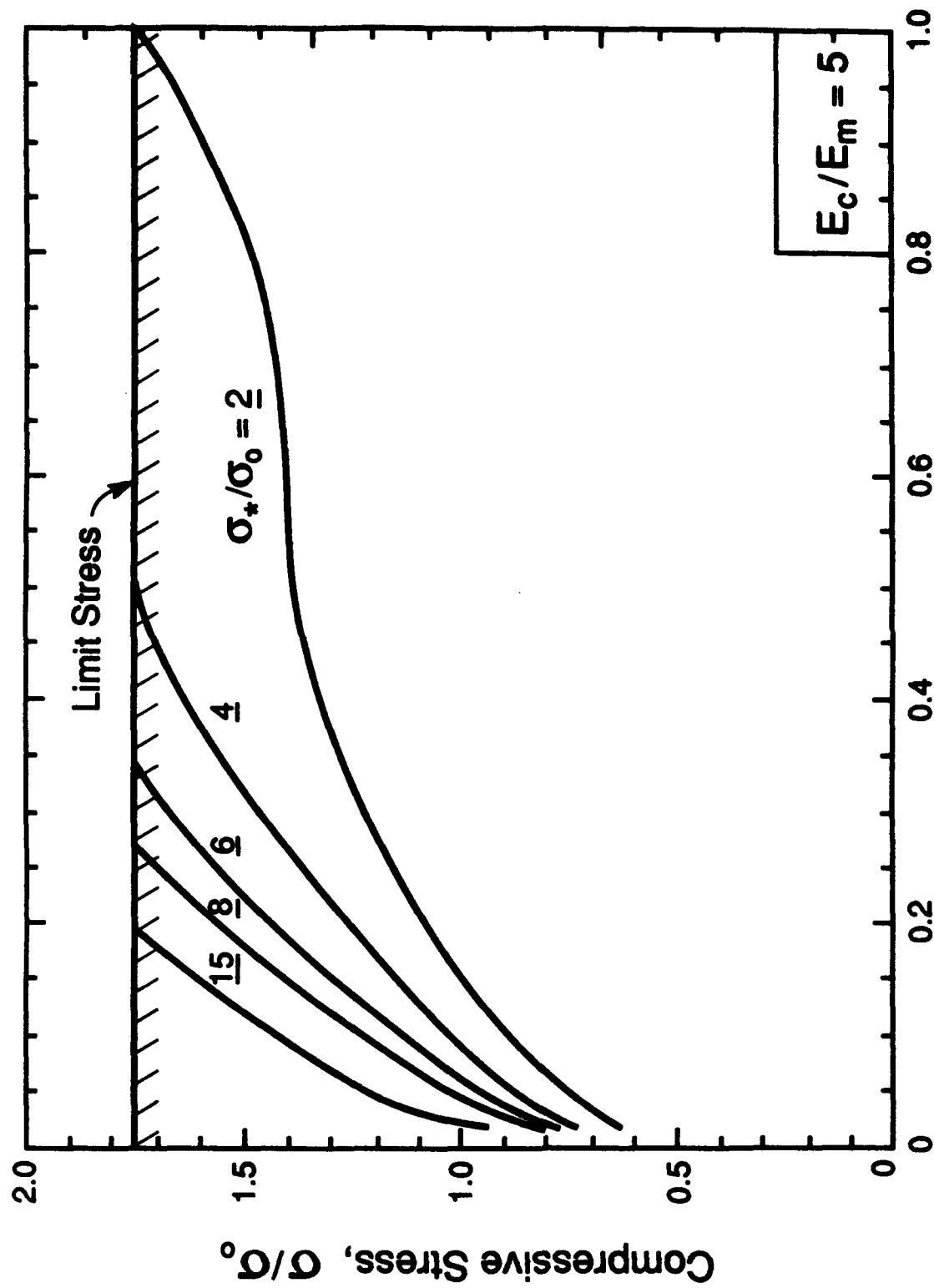


Figure 10 q



Relative Wall Thickness, t/R

Figure 10 b

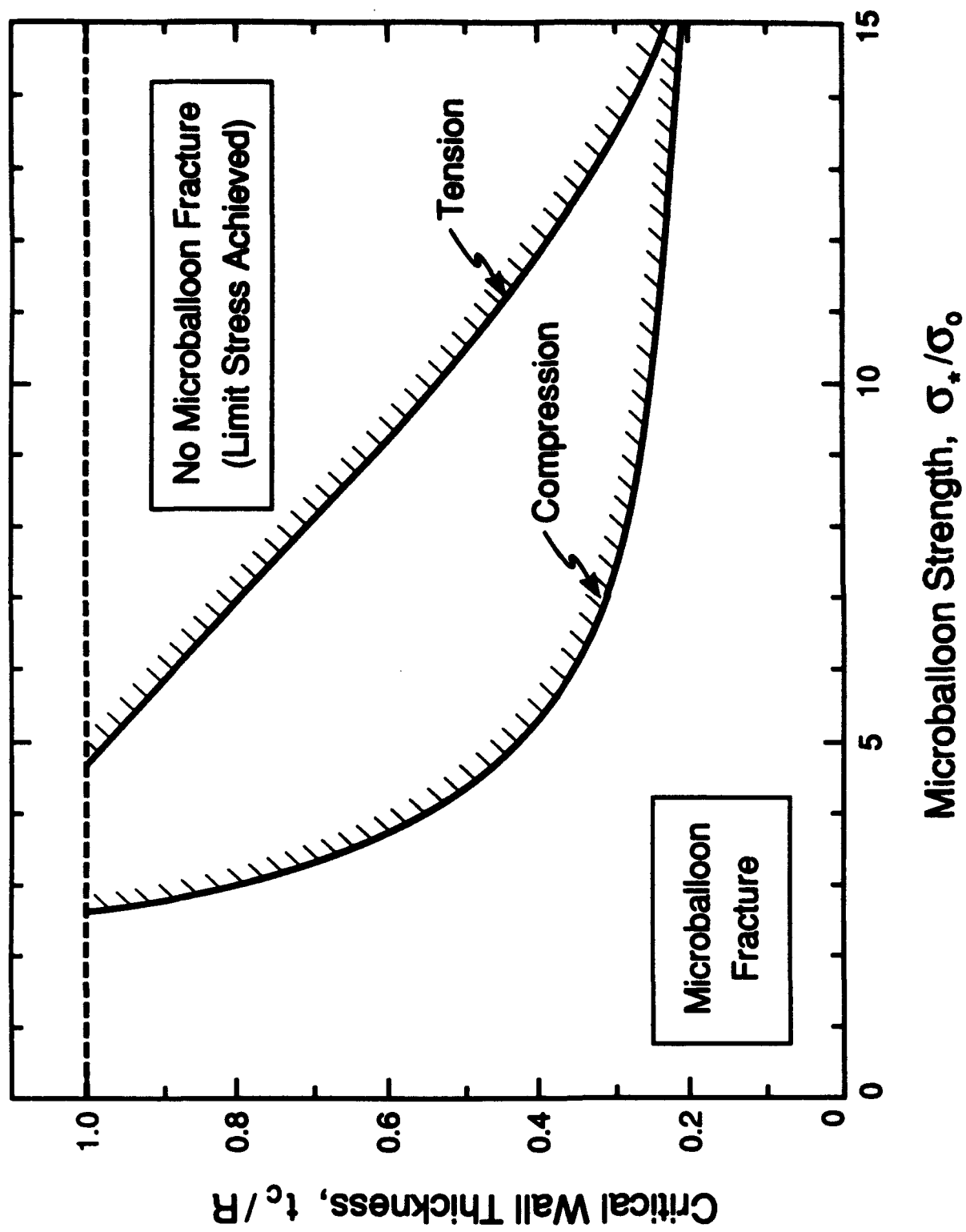


Figure 11

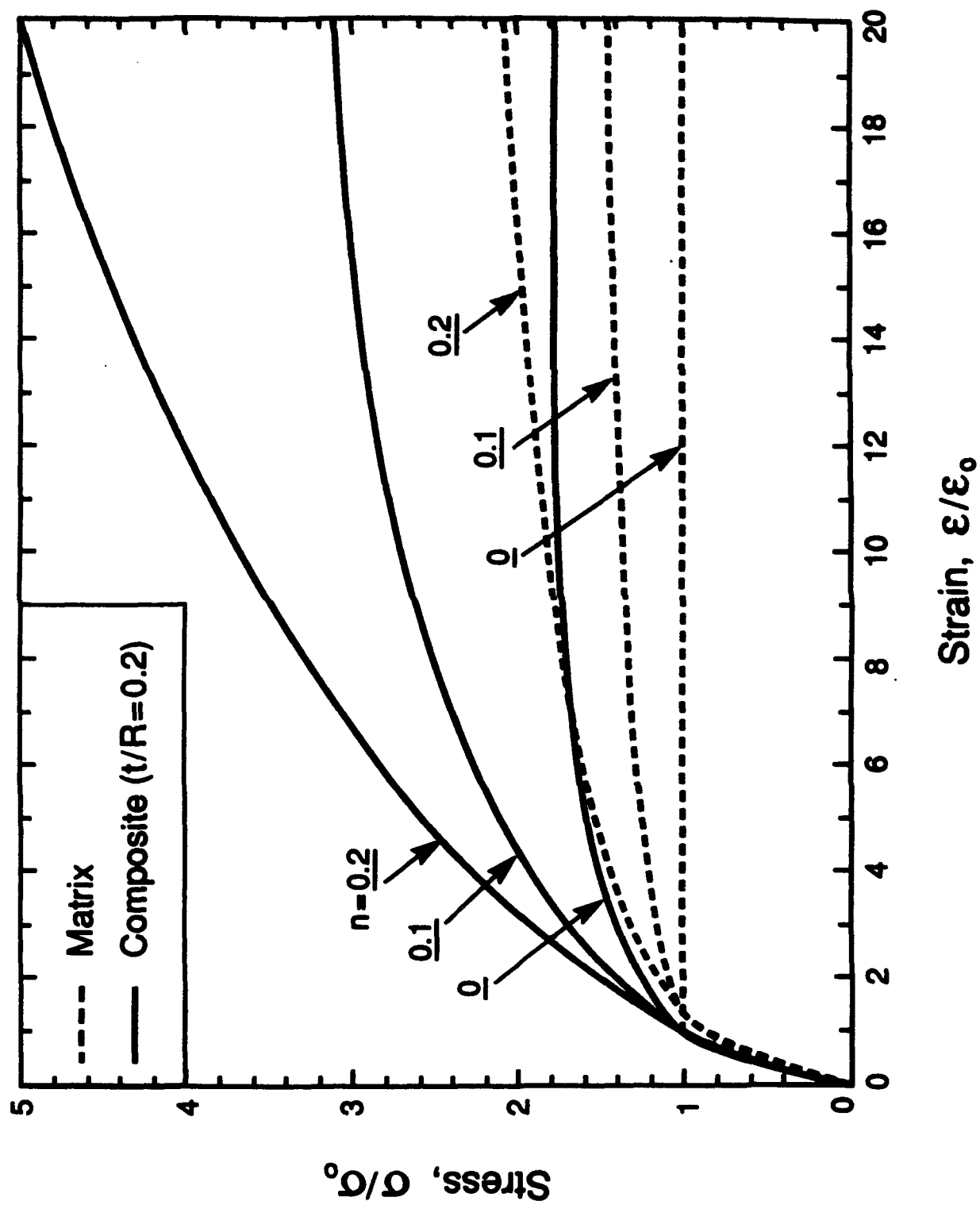


Figure 12(a)

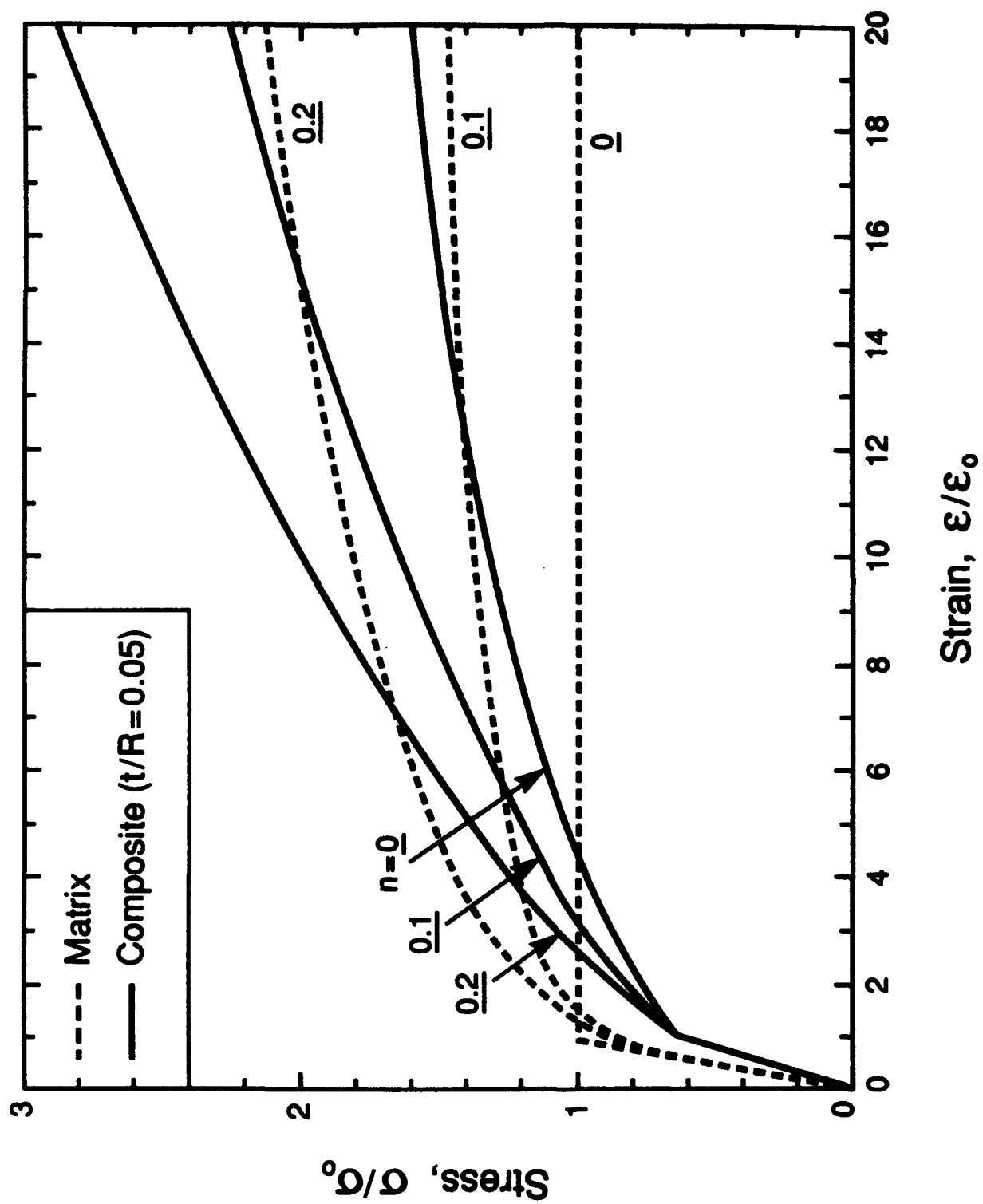


Figure 12(b)

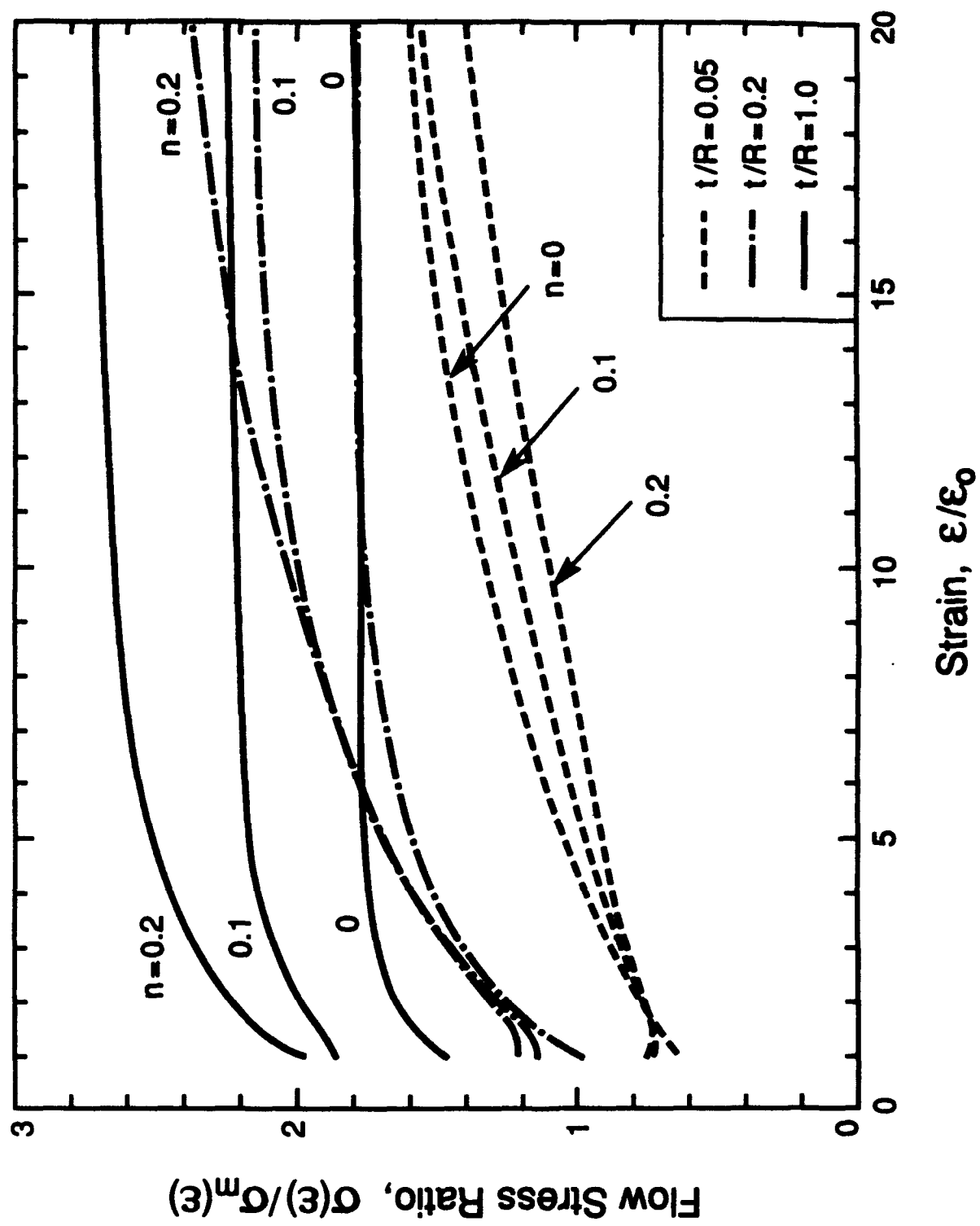


Figure 13